




# Switchable Fano Resonance Based on Cut-Induced Asymmetric Split-Ring Resonators with Dirac Semimetal Film

Dehua Tu<sup>1</sup> · Yiping Wu<sup>1</sup> · Jingya Xie<sup>1</sup> · Xiaofei Zang<sup>1</sup> · Li Ding<sup>1</sup> · Lin Chen<sup>1,2</sup> 

Received: 1 December 2020 / Accepted: 18 February 2021 / Published online: 4 March 2021  
© The Author(s), under exclusive licence to Springer Science+Business Media, LLC part of Springer Nature 2021

## Abstract

We present cut-induced asymmetric split-ring resonator (CASRR) structure that can achieve switchable Fano resonance based on Dirac semimetals at the terahertz region. By changing the asymmetric geometric parameter from 3 to 13  $\mu\text{m}$ , the transmission spectrum can be switched from single to dual channel and the Fano resonance can be gradually enhanced, which is consistent with the two coupled oscillators model. Meanwhile, the Fano effect can also be effectively switched by adjusting the Fermi energy of Dirac semimetal film (DSF) and it is suitable for practical applications. In the view of sensing application, the sensitivity based on Fano resonance is up to 69.75 GHz/RIU and 134.25 GHz/RIU with the thickness of sample 1  $\mu\text{m}$  and 20  $\mu\text{m}$ , respectively. Such manipulation of Fano resonance by using DSF may have potential applications in terahertz switch, sensor, and multichannel communication.

**Keywords** Terahertz · Dirac semimetal film · Sensitivity · Fano resonance

## Introduction

Fano resonance is a distinct asymmetric linear phenomenon in the scattering spectrum. It is in 1961 that Ugo Fano first proposed a reasonable theoretical explanation through helium and auto-ionization in a quantum system [1]. In general, Fano resonance is the result of destructive interference between the resonance with wider linewidth and the resonance with narrower linewidth. The wider linewidth is regarded as bright mode, which is easy to observe and has high radiation losses. The narrower linewidth is the dark mode because it has low radiation losses and cannot be excited directly by the light of normal incidence. Over the past decades, Fano resonance has received extensive attention in plasmonic [2–4], waveguide-coupled cavities [5, 6], and metamaterials [7–10]. Fano resonance is not only sensitive to the change of the refractive index, but also to changes

in the geometry of the structure. Hence, Fano resonance is widely used in biochemical sensors [8–11], optical switch [12–17], and nonlinear optics [18, 19].

Moreover, the study of tunability on Fano resonance has obtained extensive attention, where the property of Fano can be tuned by changing two-dimensional (2D) materials, such as doped silicon [12], germanium [13], transition metal dichalcogenides [14], perovskite [15], lead iodide [16], and graphene [20, 21]. Among this tunable method, graphene has excellent optical properties, low losses, and outstanding properties of surface conductivity due to zero-band gap. More recently, the Dirac semimetal film (DSF) is widely used to achieve tunable performance, which is known as “3D Graphene,” where bulk electrons can form three-dimensional Dirac cones and satisfy the linear dispersion relation [22, 23]. Compared with graphene, DSF is easily manufactured and stable to the environment. The Fermi energy of DSF can be adjusted by applying a gate voltage/electric currents (0–50 mA) to the Dirac semimetal layer via the two metal electrodes/wires connected [24, 25]. The change of gate voltage/electric currents can vary the temperature of DSF, resulting in the change of the carrier concentration in DSF. The Fermi level will be raised with the increasing carrier concentration of n-type DSF (for example, Cd<sub>3</sub>As<sub>2</sub>), because faster relaxation of excited electrons through electron–electron (e–e) scattering is facilitated [26]. The Fermi

✉ Lin Chen  
linchen@usst.edu.cn

<sup>1</sup> Shanghai Key Lab of Modern Optical System, University of Shanghai for Science and Technology, Shanghai 200093, People’s Republic of China

<sup>2</sup> Shanghai Institute of Intelligent Science and Technology, Tongji University, Shanghai 200092, People’s Republic of China

energy can also be adjusted by doping the alkaline metal to change the Fermi energy of the Dirac semimetal layer [27]. In fact, the charge loss can be over-compensated by K-doping, and we were observed the upper part of Dirac cone beyond the Dirac point. With the increasing of K-doping, the Fermi energy shifts upward. Hence, DSF can be widely used to tune Plasmon-induced transparency/toroidal effect [28–32], Fabry–Perot resonance [33], surface Plasmon polariton resonance [34], and guided mode [35–37]. But there are few studies on tunable Fano resonance by using DSF.

In this paper, we propose a method to actively tune Fano resonance based on cut-induced asymmetric split-ring resonator (CASRR) of DSF metamaterials at terahertz (THz) frequency. Fano resonance can be controlled by changing the asymmetric parameter or the Fermi energy of DSF, which the switch from single channel to dual channels is realized. Moreover, we make full use of advantages of DSF to realize sensing application, which can dynamically be changed the dielectric constant by changing Fermi energy. When Fermi energy is 90 meV, the sensitivity of Fano resonance can reach 69.75 GHz/RIU and 134.25 GHz/RIU under the condition of the 1- $\mu\text{m}$  and 20- $\mu\text{m}$  thickness of sample, respectively. It is important that the different sensing range can be determined by modifying the Fermi energy. Our research has great advantages in applications, such as biochemical sensors, THz switch, and other THz devices [38].

### Structure Design and Characteristics of DSF

Figure 1a shows the schematic diagram of the metamaterials structure for realizing Fano effect. The structure consists of two layers: a lossy substrate of polyimide with a permittivity of  $3.5 + 0.0027i$  and cut-induced asymmetric split-ring resonator based on DSF, where the thickness is  $h = 25 \mu\text{m}$  and  $t = 0.2 \mu\text{m}$ , respectively. One unit cell of the designed Fano structure is shown in Fig. 1b, where

the unit cell parameters are as follows:  $P_x = P_y = 90 \mu\text{m}$ ,  $r = 24 \mu\text{m}$ ,  $R = 30 \mu\text{m}$ , the  $w$  is  $2 \mu\text{m}$ , and the asymmetry parameter  $S$  represents the offset length. The incident waves with magnetic and electric field polarized along the  $x$  and  $y$  directions irradiate normally to the surface of the structure. The Kubo formula controls the complex surface conductivity of the DSF, and using the random phase approximation at the long-wavelength limit, the real and imaginary conductivities of the Dirac semimetal are expressed as follows [22]:

$$\text{Re}\sigma(\Omega) = \frac{e^2}{\hbar} \frac{gk_F}{24\pi} \Omega G(\Omega/2) \tag{1}$$

$$\text{Im}\sigma(\Omega) = \frac{e^2}{\hbar} \frac{gk_F}{24\pi^2} \left[ \frac{4}{\Omega} \left( 1 + \frac{\pi^2}{3} \left( \frac{T}{E_F} \right)^2 \right) + 8\Omega \int_0^{\epsilon_c} \left( \frac{G(\epsilon) - G(\Omega - 2)}{\Omega^2 - 4\epsilon^2} \right) \epsilon d\epsilon \right] \tag{2}$$

where  $G(E) = (-E) - n(E)$ ,  $\epsilon = E/E_F$ ,  $n(E)$  is Fermi distribution function,  $E_F$  is the Fermi energy,  $\epsilon_c = E_c/E_F$ ,  $k_F = E_F/\hbar v_F$ ,  $v_F = 10^6 \text{m/s}$   $v_F$  is the Fermi velocity,  $k_F$  represents the Fermi momentum,  $\Omega = \hbar\omega/E_F$ ,  $E_c = 3$  is the cut-off energy, and  $g$  is the degeneracy factor. The permittivity of the Dirac semimetals can be written as follows [22]:

$$\epsilon = \epsilon_b + i\sigma/\omega\epsilon_0 \tag{3}$$

where  $\epsilon_b = 1$  for  $g = 40$  (AlCuFe quasicrystals [39]) and  $\epsilon_0$  is the permittivity of the vacuum. According to the above permittivity equation of Dirac semimetals, the real and imaginary parts of permittivity under different frequency were calculated. Figure 2a, b show that the DSF permittivity is related to the frequency and Fermi energy. The real part of permittivity increases with the frequency, and it is below zero at the 0~2.5 THz as shown in Fig. 2a. It indicates that the properties of DSF are similar to metal at the 0~2.5 THz.

**Fig. 1** (a) Part schematic tunable Fano effect based on DSF metamaterials. (b) One unit of the DSF structure. The geometry parameters are as follows:  $P_x = P_y = 90 \mu\text{m}$ , the inner radius is  $r = 24 \mu\text{m}$ , the outer radius is  $R = 30 \mu\text{m}$ , the thickness of polyimide is  $h = 25 \mu\text{m}$  and the thickness of DSF  $t = 0.2 \mu\text{m}$

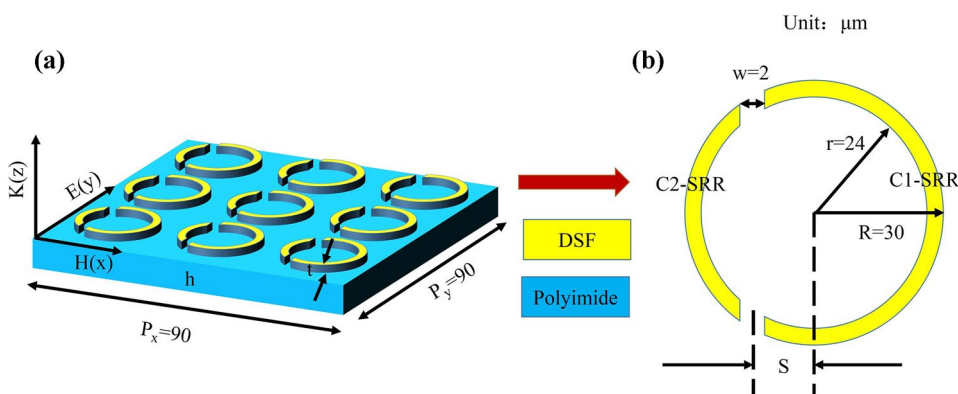
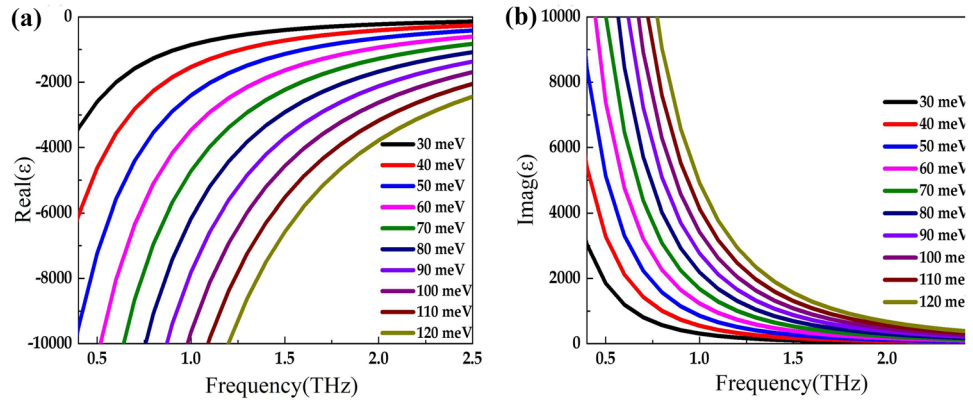


**Fig. 2** (a) The real part of DSF permittivity under different Fermi energy. (b) The imaginary part of DSF permittivity under different Fermi energy



### Two Coupled Oscillators Model and Simulation

Figure 3 shows the transmission spectra of the individual longer C1-SRR, shorter C2-SRR, and coupled CASRR system under the condition of asymmetry parameter  $S = 13 \mu\text{m}$  and  $E_F = 90 \text{ meV}$ . The C1-SRR is directly excited by the external field as a bright mode, and C2-SRR could be treated as an indirectly excited dark SRR because its eigen resonance frequency is far from the Fano resonance frequency. The dark C2-SRR is excited by the magnetic flux of the bright C1-SRR via the near field interaction. In this CASRR, the Fano resonance phenomenon at smaller resonance comes from the interference between the broadband coupled dipole mode of longer C1-SRR (as a continuum) and the leaky mode defined as the difference in the surface currents between the C1-SRR and C2-SRR arms [7]. To see this clearly, we also investigated the surface current distribution at the Fano resonance frequency to verify the coupling

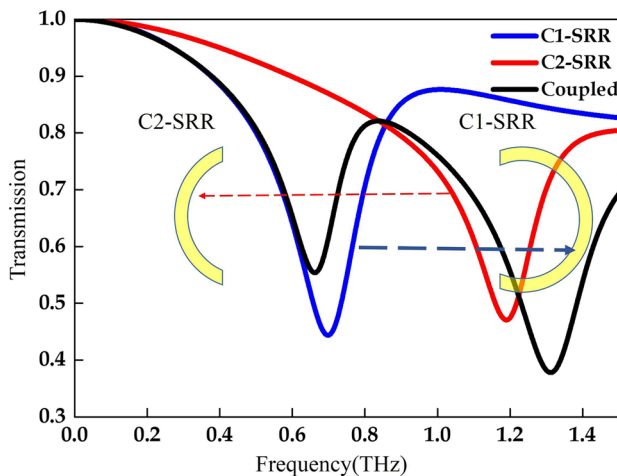


**Fig. 3** Simulated transmission spectra of separate C1-SRR, C2-SRR, and the coupled cut-induced asymmetric SRR system when  $S = 13 \mu\text{m}$

effect as shown in Fig. 4. The more different the surface currents between the C1 and C2-SRR arms are, the stronger the Fano resonance is. In addition, the strong antiparallel surface currents in the C1-SRR and C2-SRR form a closed loop that can be observed at the Fano resonance while the incident electric field polarizes parallel to the vertical gaps. This phenomenon is attributed to the magnetic coupling in the system.

The formation of Fano resonance can be calculated by two coupled oscillator model. Here the two coupled resonators are the individual longer C1-SRR and shorter C2-SRR. The vibration displacement of the two oscillators satisfies the second order partial differential equation:

$$\ddot{x}_b(t) + \gamma_b \dot{x}_b(t) + \omega_b^2 x_b(t) + \eta^2 x_b(t) = f_b E \tag{4}$$

$$\ddot{x}_d(t) + \gamma_d \dot{x}_d(t) + \omega_d^2 x_d(t) + \eta^2 x_d(t) = 0 \tag{5}$$

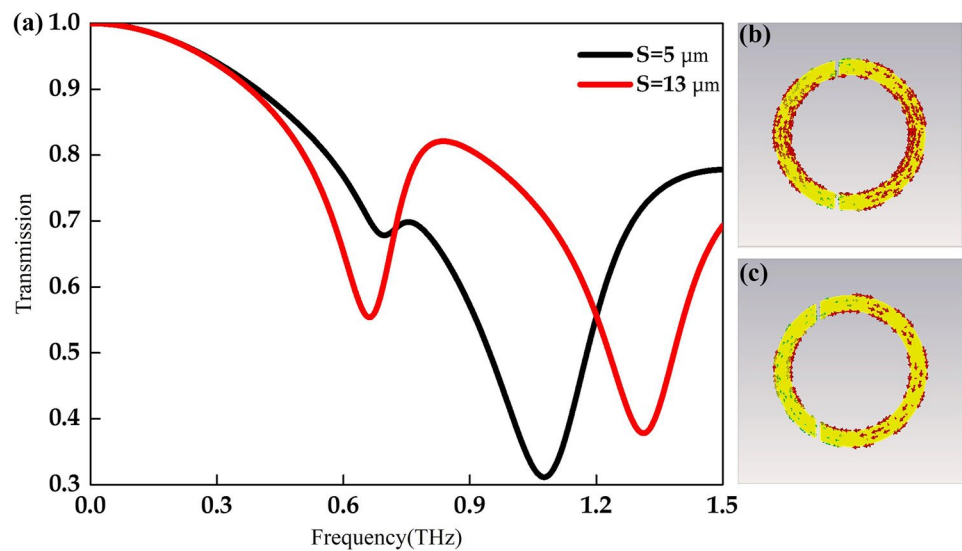
where  $(x_b, x_d)$ ,  $(\omega_b, \omega_d)$  and  $(\gamma_b, \gamma_d)$  are the scattering amplitudes, angular resonance frequency, and the linewidth of two oscillators, respectively.  $\eta$  represents the coefficient of coupling between two oscillators.  $f_b$  is the periodic driving force applied to the oscillator. After solving for the scattering amplitudes in the coupled equation, one can arrive at the susceptibility expression for light-matter interaction given by the following [40]:

$$\chi = K \left( \frac{(\omega^2 - \omega_d^2) + i\omega\gamma_d}{\eta^4 - (\omega^2 - \omega_d^2 + i\omega\gamma_d)(\omega^2 - \omega_b^2 + i\omega\gamma_b)} \right) \tag{6}$$

The real part ( $Re[\chi]$ ) represents the dispersion, and the imaginary part ( $Im[\chi]$ ) represents the losses in the system, where  $K$  is the normalizing coefficient.  $1-Im[\chi]$  is the transmission spectrum, and the coupling strength  $\eta$  determines the intensity of Fano resonance, which is related to the asymmetric parameter  $S$  in the metamaterial structure.

Therefore, we can study the influence of the asymmetry parameter  $S$  on the structure when the Fermi energy is fixed to 90 meV, both in theory and in simulation. The simulated

**Fig. 4** (a) Simulated transmission spectrum with  $S=5\ \mu\text{m}$  and  $S=13\ \mu\text{m}$ . Simulated surface current distribution at the Fano resonance, while (b)  $S=5\ \mu\text{m}$  and (c)  $S=13\ \mu\text{m}$



results are modelled through Computer Simulation Technology (CST) Microwave Studio software at the frequency domain solver. The boundary conditions set unit cell in  $x$ - $y$  position and open in the  $z$  position, respectively. Moreover, the simulation and theoretical results obtained by two coupled oscillators model are shown in Fig. 5a, b. In the original state, CASRR with  $S$  value of  $3\ \mu\text{m}$  shows single-resonance at  $1.060\ \text{THz}$  as shown in Fig. 5a. When  $S$  value equals to  $5\ \mu\text{m}$ , it exhibits dual-resonance at  $0.697\ \text{THz}$  and  $1.075\ \text{THz}$  for the first and second resonances, respectively. When  $S$  value is adjusted from  $5$  to  $13\ \mu\text{m}$ , the first resonance is gradually enhanced. We note that the first resonance is Fano resonance and the second resonance is dipole resonance. In Fig. 5a, b, the strength of the Fano resonance strongly depends on the asymmetry parameter  $S$ . To better understand the physical mechanism behind this, we use the two coupled resonators model to analyze it. We find that the coupling coefficient  $\eta$  in the model is linear to the asymmetry parameter  $S$ , as shown in Fig. 5c. This comparison further confirms that the Fano resonance is the inductive coupling in the leaky mode and the coupled dipole mode. The strength of the coupling is determined by the location of the eigen resonance frequency of the individual C1 (C2)-SRR. We also plot the Fano resonance frequency with different asymmetries in Fig. 5e, where the black and red lines represent simulation and theoretical results, respectively. It demonstrates the relevance between the frequency of Fano resonance and asymmetry parameter, which illustrates that the resonance frequency redshifts as asymmetry parameter increasing. It is concluded that the Fano intensity varies from  $0.02$  to  $0.267\ \text{THz}$  and grows linearly as the asymmetry parameter  $S$  increases in Fig. 5f. To actively describe the tunable process under different asymmetry parameter  $S$ , we plot the transmission map as a function of asymmetry

parameter  $S$  in Fig. 6. The low-frequency resonance is Fano resonance; the high-frequency resonance represents dipole resonance. We can obtain that the Fano resonance can be excited at around  $S=5\ \mu\text{m}$ . The Fano intensity is enhanced with the asymmetry parameter  $S$  increasing. The results indicate that the transmission spectrum though altering the asymmetry parameter  $S$  not only exhibits the tunability from single channel to dual channel but also enhances the Fano resonance.

We also study the influence of the width of gaps  $w$  on the structure. The relationship between different width of gap and transmission spectra is shown in Fig. 7a. Other parameters are as follows:  $S=13\ \mu\text{m}$ , and  $E_f=90\ \text{meV}$ . Result illustrates that the low resonance frequency (Fano) blueshifts, and the bandwidth of Fano resonance becomes broad as gap width increased, resulting in low Q-factor. This is because the larger the gap width is, the weaker the energy confinement in the gap is. So we chose small gap width to enhance the energy confinement. Figure 7b shows simulated transmission spectra of CASRR for TE (magnetic field polarized along the  $x$  direction and electric field polarized along the  $y$  direction) and TM (magnetic field polarized along the  $y$  direction and electric field polarized along the  $x$  direction) polarizations. Results demonstrated that Fano resonance can only be excited for TE polarization. In this situation, the electric field can be effectively coupled to C1-SRR arm and C2-SRR arm, which are closely related to Fano resonance. However, for TM polarization, the electric field is perpendicular to C1-SRR and C2-SRR arms, resulting in dipole resonance in the transmission spectrum.

In the above discussion, we can see that the stronger the Fano resonance is, the more different the surface currents between the C1-SRR and C2-SRR arms are (Fig. 4b, c). This leads to the interaction between dipole mode and leaky



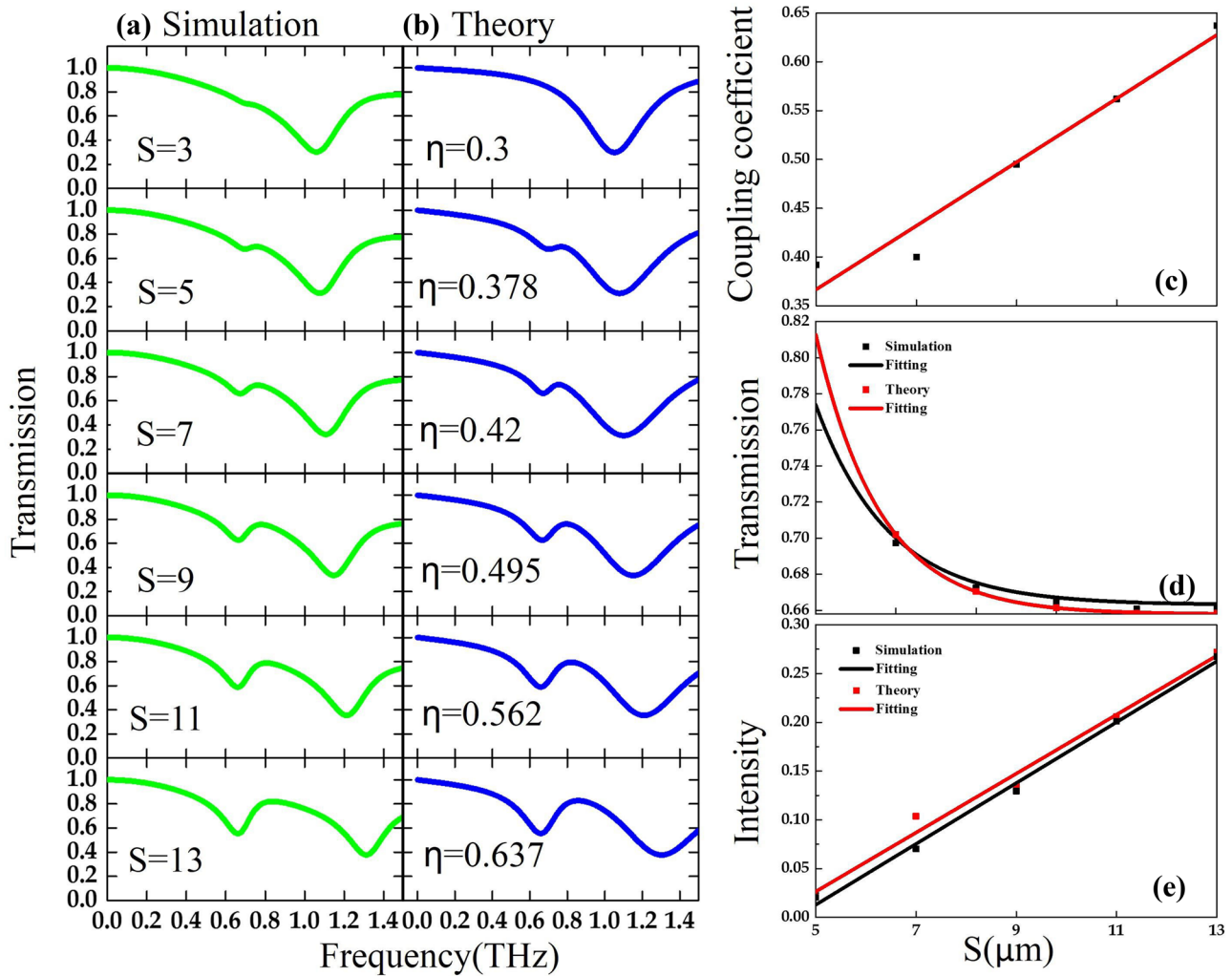


**Fig. 5** (a) Transmission spectrum of DSF with different asymmetry parameter  $S$  from 3 to 13  $\mu\text{m}$ . (b) Transmission spectrum of DSF simulated by theoretical formula. (c) The coupling coefficient  $\eta$  with dif-

ferent asymmetry parameters  $S$ . (d) Fano resonance frequency with respect to different asymmetry parameters  $S$ . (e) Fano intensity with respect to different asymmetry parameters  $S$

mode. Interestingly, the electric field at the gaps increases distinctly with the asymmetry parameter  $S$  increasing, as shown in Fig. 8c, d. When  $S = 3$   $\mu\text{m}$ , dipole mode can only be excited and the transmission spectrum are shown in Fig. 8a; the C1 and C2 resonators generate parallel currents, the electric field distributes along the arms and is very weak in the gap (Fig. 8c). As  $S$  increases, in addition to the dipole mode, a Fano mode, which the C1 and C2 resonators generate a reverse parallel current and form a closed loop current, shows a magnetic dipole mode (Fig. 4b, c). When  $S = 13$   $\mu\text{m}$ , the two gaps behave as effective capacitors and the transmission spectrum is shown in Fig. 8b. We can observe the accumulation of opposite charges due to the capacitance

effect and the electric field are confined in the gaps at the Fano resonance (Fig. 8d). The more  $S$  increases, the stronger the magnetic dipole mode is, and the more confinement the electric field is in the gaps.

On the one hand, when the structure we proposed has been fabricated, it is hardly to change the resonance frequency by adjusted asymmetry parameter. On the other hand, the resonance frequency can be tuned by varying the surface conductivity of DSF. Moreover, the change of Fermi energy leads to the change of surface conductivity. Therefore, we explored the influence of different Fermi energy for the transmission spectrum under the condition of  $S = 9$   $\mu\text{m}$ . The relationship between different Fermi

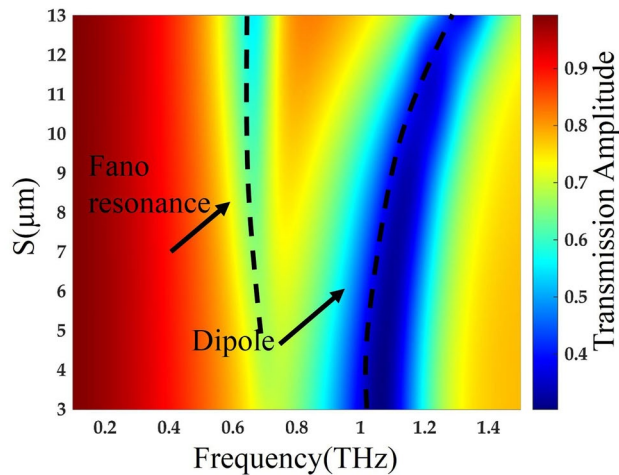


**Fig. 6** Transmission spectrum map as a function for asymmetry parameter  $S$

energy and transmission spectrum is shown in Fig. 9a. It is clearly observed the tunable process from single channel to dual channel in the transmission spectrum. In the original state, the transmission spectrum has only dipole resonance when the Fermi energy is below 60 meV. When the Fermi energy is larger than 60 meV, the transmission spectrum shows dual-resonance, which are dipole resonance and Fano resonance, respectively. What's more, the Fano resonance frequency shifts to the higher frequency (blue shift) with the Fermi energy increasing as shown in Fig. 9b. The Fano frequency changes 0.212 THz from 0.568 to 0.780 THz. In Fig. 9c, the Fano intensity linearly increases with the increasing of Fermi energy, where the resonance intensity varies from 0.017 to 0.29 THz. Similarly, we also plot the transmission map as a function of Fermi energy in Fig. 10.

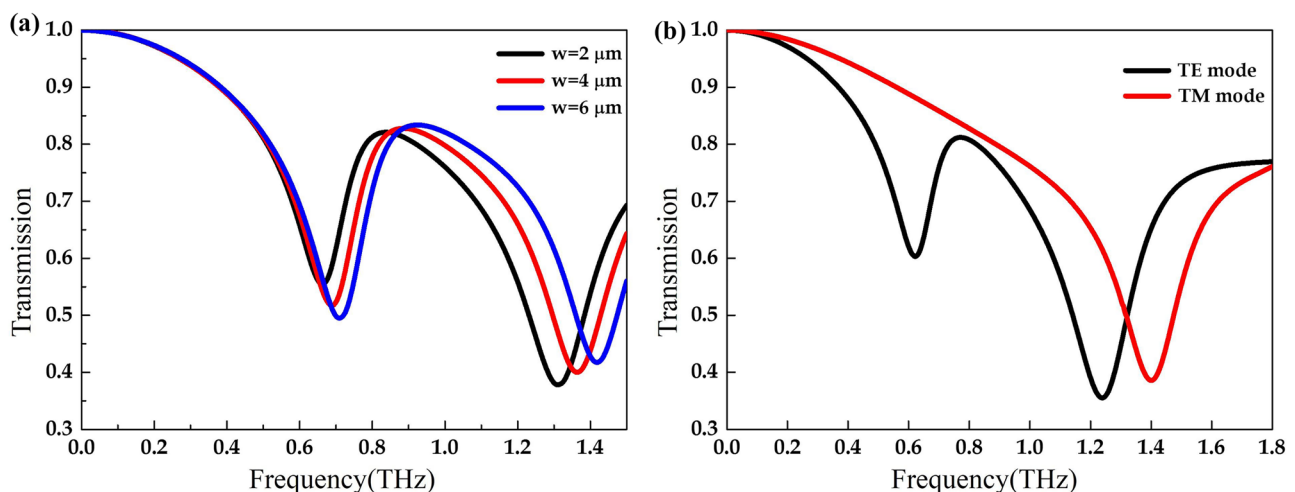


**Fig. 7** (a) Simulated transmission spectra with respect to different gap width when  $S = 13 \mu\text{m}$ . (b) Simulated transmission spectra with respect to TE mode and TM mode

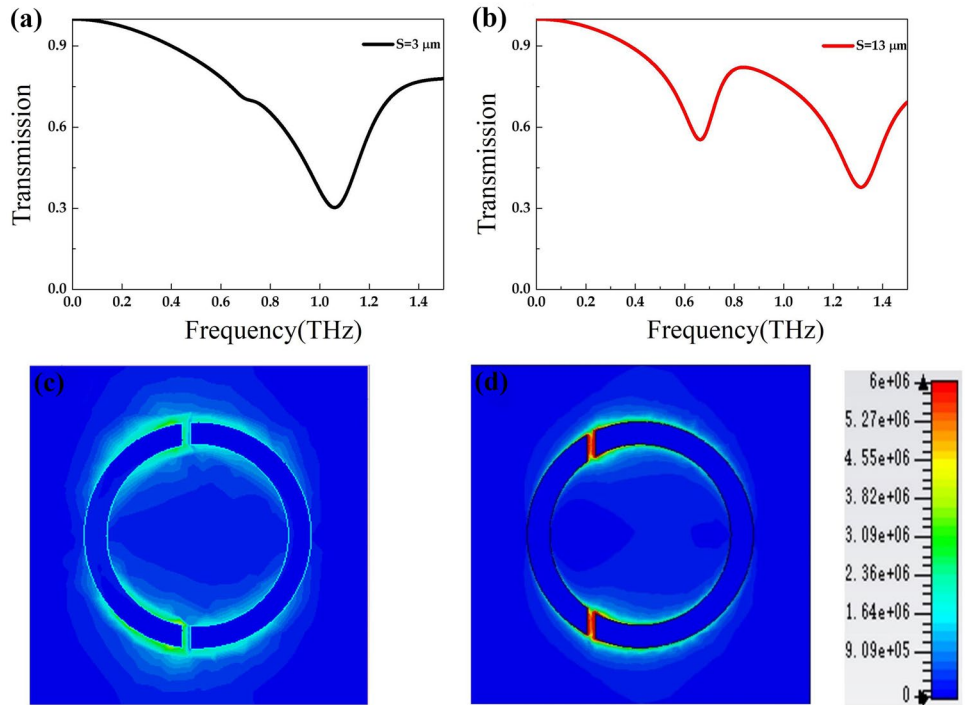
Obviously, it can be seen that the Fano resonance can be excited when Fermi energy is larger 60 meV and the dipole resonance always exists in the transmission spectrum.

We also obtain the electric field distribution of Fano resonance under the Fermi energy of 30 meV, 50 meV, and 70 meV, respectively, as shown in Fig. 11. In the original state, when Fermi energy equals to 30 meV, the transmission spectrum has only dipole resonance at 0.583 THz in Fig. 11a. Because there is no capacitance effect in the structure gaps, which does not lead to Fano resonance in Fig. 11d, when Fermi energy is 50 meV, the electric field in the structure gaps is weaker in Fig. 11e. Therefore, the transmission spectrum shows that Fano resonance is not excited. When the Fermi energy equals to 70 meV, the electric field mainly concentrated at the gaps of the structure, as shown in Fig. 11f. The transmission spectrum shows Fano resonance at 0.607 THz and dipole resonance at 1.018 THz. This is because that the gaps in the structure produce the capacitance effect, where the charges due to the oscillating current accumulate and enhance the field strength within the gaps [12]. From the above analysis, we observe that the electric field at the gaps increases distinctly with the growth of Fermi energy, which leads to Fano resonance on the transmission spectrum.

## Sensing Application

In order to realize the sensing application, we add a layer of sample with different refractive indices on the CASRR structure. First, we define that the asymmetry parameter of structure equals to  $9 \mu\text{m}$ , the Fermi energy equals to 90 meV, the thickness of the sample equals to  $1 \mu\text{m}$ , and the sample covers the whole structure ( $90 \mu\text{m} \times 90 \mu\text{m}$ ), as

**Fig. 8** (a) Transmission spectrum with asymmetry parameter  $S$  is  $3 \mu\text{m}$ . (b) Transmission spectrum with asymmetry parameter  $S$  is  $13 \mu\text{m}$ . (c) When asymmetry parameter  $S$  is  $3 \mu\text{m}$ , electric field distribution of the dipole resonance at  $1.060 \text{ THz}$ . (d) When asymmetry parameter  $S$  is  $13 \mu\text{m}$ , electric field distribution of the Fano resonance at  $0.666 \text{ THz}$



shown in Fig. 12a. Figure 12b exhibits the transmission spectrum with different refractive indices of sample from 1 to 1.8. These results show that the frequency of Fano

resonance shows red-shift with the increasing of refractive index. Moreover, we plot the relationship between the resonance shift and different refractive indices and calculate

**Fig. 9** (a) Transmission spectra with different Fermi energy. (b) The frequency of Fano resonance with different Fermi energy. (c) Fano resonance intensity with different Fermi energy

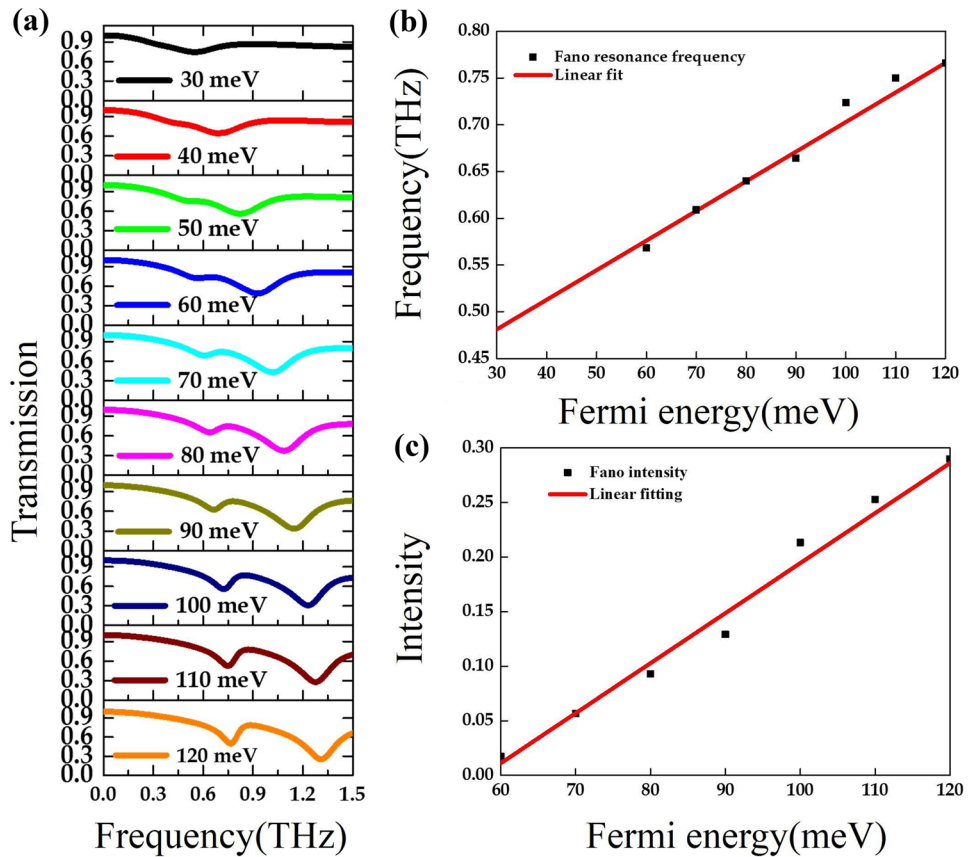
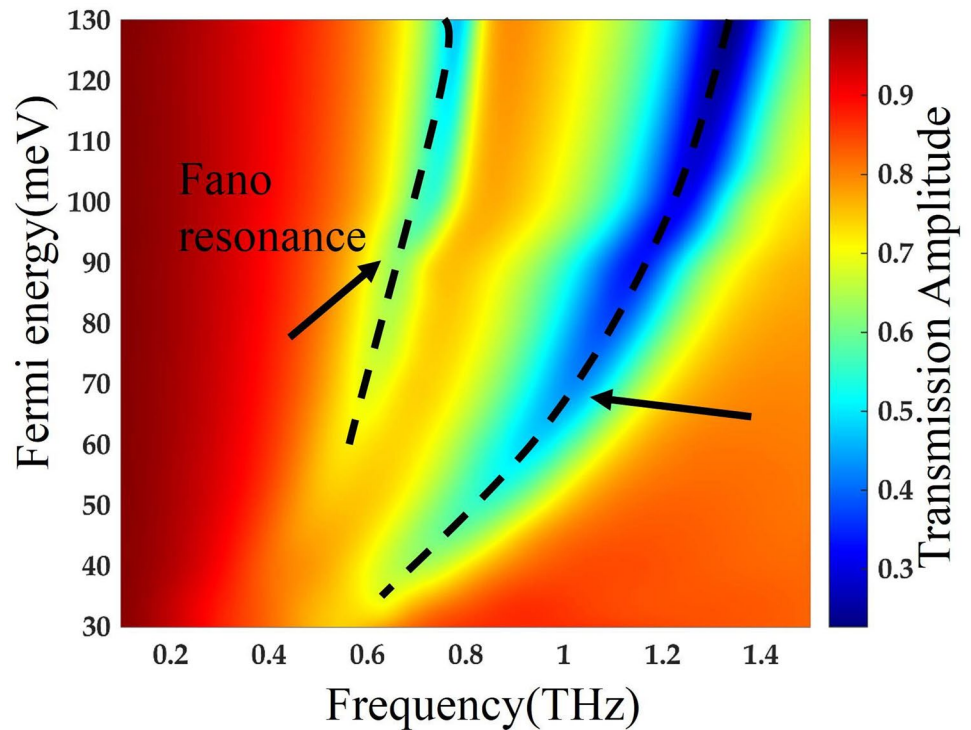


**Fig. 10** Transmission spectra as a function for Fermi energy



the sensitivity, as shown in Fig. 12c, where the sensitivity is defined as  $\Delta f/\Delta n$  ( $f$  and  $n$  are the resonance frequency and refractive index of sample). The Fano resonance sensitivity can reach 69.75 GHz/RIU. We next discuss the effect

of sample thickness on sensitivity as shown in Fig. 12d. It is obvious that the sensitivity becomes larger with the increasing of sample thickness. When the thickness of samples equals to 20  $\mu\text{m}$ , the Fano sensitivity can reach

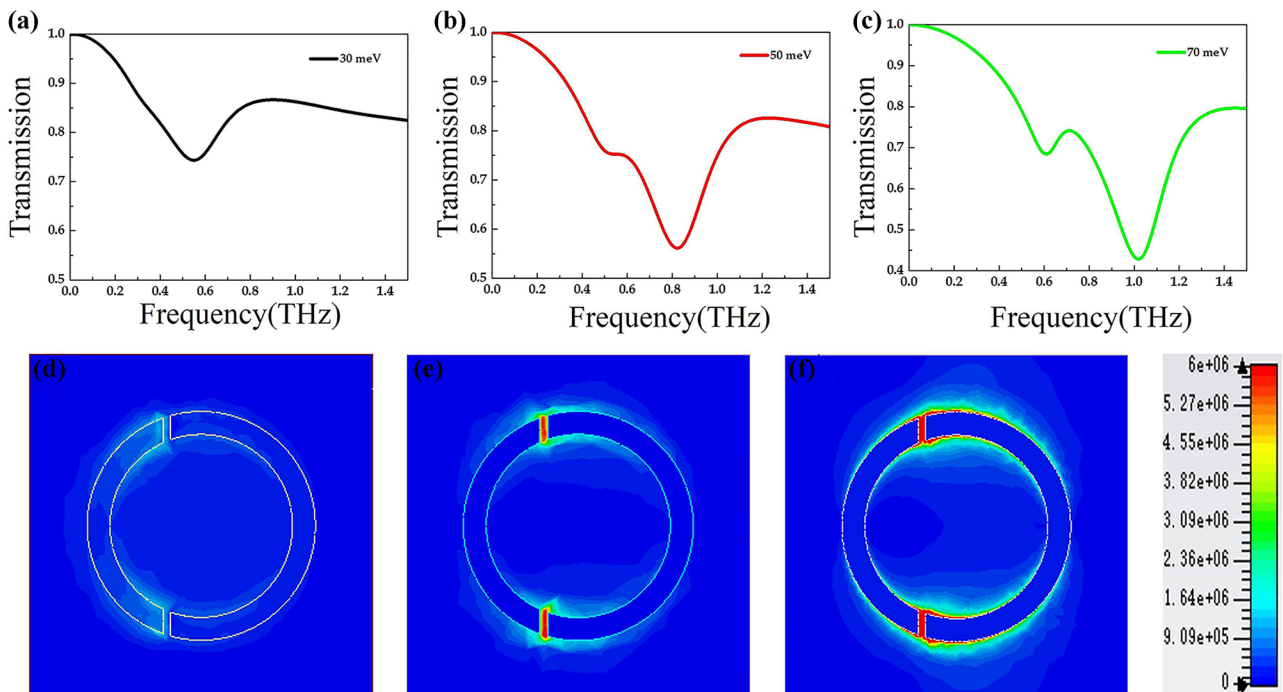
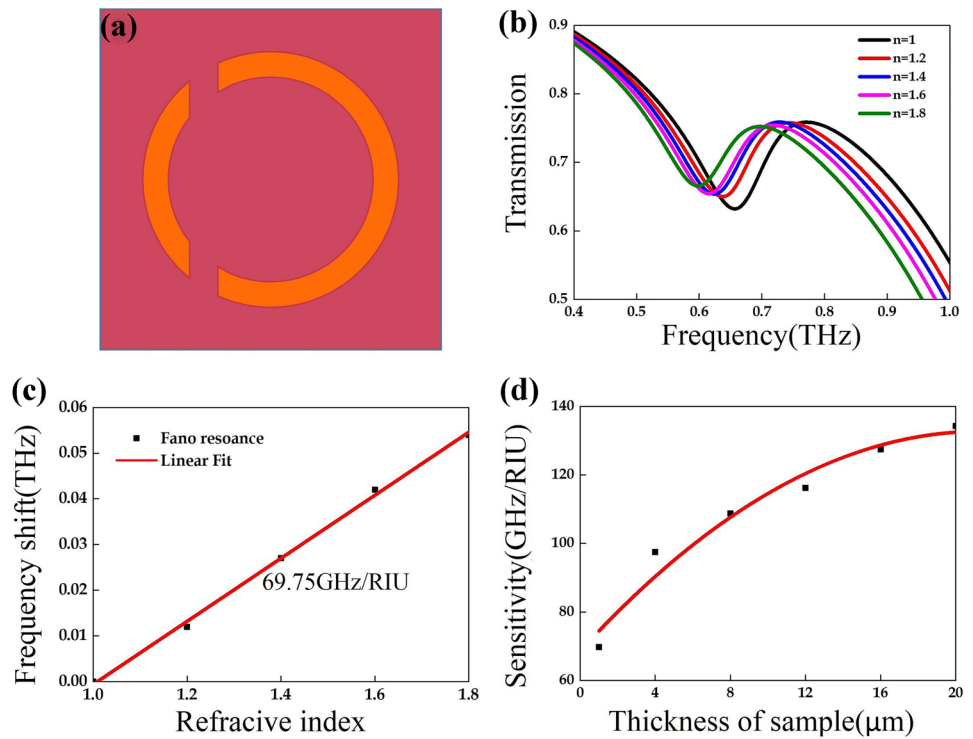


**Fig. 11** Transmission spectra at the Fermi energy is 30 meV (a), 50 meV (b) and 70 meV (c), respectively, and the electric field distribution of Fano resonance at the 0.481 THz (d), 0.544 THz (e) and 0.607 THz (f), respectively



**Fig. 12** (a) The sample covers the whole structure ( $90 \times 90 \mu\text{m}$ ). (b) Transmission spectra of Fano resonance when  $1 \mu\text{m}$  thickness sample with different refractive indices is coated on the structure. (c) Fano frequency shifts with different refractive indices. (d) The sensitivity of Fano resonance with different refractive indices of samples by changing the thickness of samples



134.25 GHz/RIU. Therefore, we can adjust the thickness of sample to realize enhancement of sensitivity.

We also find that the Fano resonance sensitivity is 69.75 GHz/RIU and the dipole resonance sensitivity can reach 67.2 GHz/RIU when the whole area ( $90 \times 90 \mu\text{m}$ ) of the sensor is covered with the sample, as shown in Fig. 13. The sensitivity of Fano resonance is a little higher than dipole resonance. However, the physical origin behind these two modes is different. The frequency shift of the dipole mode is caused by a slight change in the optical

length of the C1-SRR and C2-SRR split resonators. To see this clearly, we do the simulation where the sample is only coated near two gaps (covering the two spots, each is  $9 \times 9 \mu\text{m}$ ) [41], as shown in Fig. 14. The sensitivity of Fano resonance is 51 GHz/RIU, and the sensitivity of dipole resonance is 45.75 GHz/RIU in the case of the sample covering two spots only at the CASRR. The sensitivity of Fano resonance is higher than that of dipole resonance. We note that the volume of the sample in Fig. 14 is much less than that in Fig. 13.

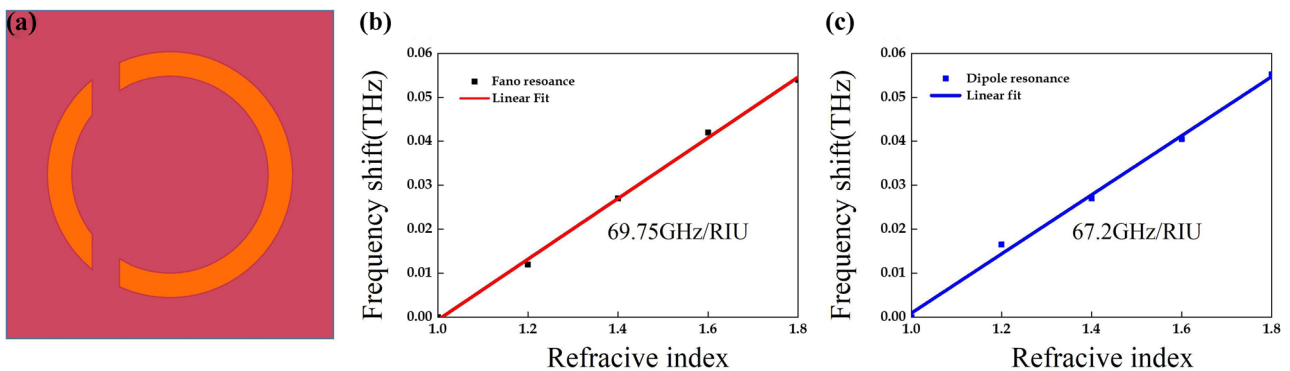


**Fig. 13** (a) The sample covers the whole area ( $90 \times 90 \mu\text{m}$ ). (b) Fano frequency shifts with different refractive indices at the whole area. (c) The dipole resonance frequency shifts with different refractive indices at the whole area

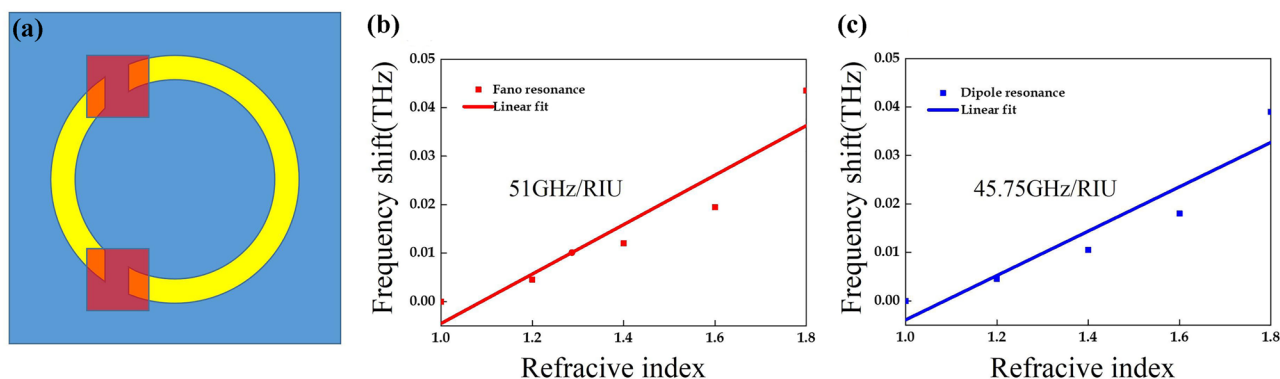


**Fig. 14** (a) The sample covers the two spots at the SRR gaps ( $9 \times 9 \mu\text{m}$ ). (b) Fano frequency shifts with different refractive indices at the SRR gaps ( $9 \times 9 \mu\text{m}$ ). (c) The dipole resonance frequency shifts with different refractive indices at the SRR gaps ( $9 \times 9 \mu\text{m}$ )

## Conclusion

In conclusion, we have successfully proposed CASRR structure based on DSF, which can be effectively tuned at the terahertz region. The transmission spectrum not only is related to the asymmetry of structure but also can be tuned by Fermi energy of DSF. In terms of asymmetry, results show that the transmission spectrum can show dual channel, which are Fano resonance and dipole resonance. Moreover, Fano resonance enhances with the increasing of asymmetry, which is basically consistent with the theoretical results. We also demonstrate that the transmission spectrum can be dynamically tuned by changing the Fermi energy of DSF. Meanwhile, we realize the sensitivity of 69.75 GHz/RIU with Fano resonance under the condition of  $1 \mu\text{m}$  thickness of sample and can reach 134.25 GHz/RIU by changing sample thickness. Hence, this results may provide a new method in designing THz sensing, active switching, and other THz devices.

**Author Contribution** All authors contributed to the study. Simulation was performed by Dehua Tu and Yiping Wu. Methodology and formal analysis were performed by Jingya Xie. Supervision and validation were performed by Xiaofei Zang. Data verification and writing—review and editing were performed by Li Ding. Conceptualization, writing—original draft, review, and editing were performed by Lin Chen. All authors read and approved the final manuscript.

**Funding** This project was supported by the National Key R&D Program of China (2018YFF01013003), the National Natural Science Foundation of China (Nos. 61671302, 61988102), the Shuguang Program Supported by Shanghai Education Development Foundation and Shanghai Municipal Education Commission, China (No. 18SG44), the 111 Project (D18014), and the International Joint Lab Program supported by Science and Technology Commission Shanghai Municipality (17590750300).

**Data Availability** The datasets generated during and/or analyzed during the current study are available from the corresponding author on reasonable request.

## Declarations

**Competing Interests** The authors declare that they have no conflict of interest.

**Consent to Participate** Informed consent was obtained from all authors.

**Consent for Publication** The authors confirm that there is informed consent to the publication of the data contained in the article. We confirm that this work is original and has not been published elsewhere, nor is it currently under consideration for publication elsewhere.

## References

1. Fano U (1961) Effects of configuration interaction on intensities and phase shifts. *Phys Rev* 124:1866–1878. <https://doi.org/10.1103/physrev.124.1866>
2. Chen L, Zhu Y, Zang X, Cai B, Li Z, Xie L, Zhuang S (2013) Mode splitting transmission effect of surface wave excitation through a metal hole array, *Light: Sci Appl* 2:e60. <https://doi.org/10.1038/lsa.2013.168>
3. Chen L, Xu N, Singh L, Cui T, Singh R, Zhu Y, Zhang W (2017) Defect-induced Fano resonances in corrugated plasmonic metamaterials. *Adv Opt Mater* 5:1600960. <https://doi.org/10.1002/adom.201600960>
4. Luk'Yanchuk B, Zheludev NI, Maier SA (2010) The Fano resonance in plasmonic nanostructures and metamaterials. *Nat Mater* 9:707–715. <https://doi.org/10.1038/nmat2810>
5. Chen L, Cao Z, Ou F, Li H, Shen Q, Qiao H (2007) Observation of large positive and negative lateral shifts of a reflected beam from symmetrical metal-cladding waveguides, *Opt Lett* 32:1432–1434. <https://doi.org/10.1364/OL.32.001432>
6. Chen L, Gao C, Xu J, Zang X, Cai B, Zhu Y (2013) Observation of electromagnetically induced transparency-like transmission in terahertz asymmetric waveguide-cavities systems, *Opt Lett* 38:1379–1381. <https://doi.org/10.1364/OL.38.001379>
7. Fedotov VA, Rose M, Prosvirnin SL, Papasimakis N, Zheludev NI (2007) Sharp dark-mode resonances in planar metamaterials with broken structural symmetry. *Physics* 99:12243–12254. <https://doi.org/10.1103/PhysRevLett.99.147401>
8. Cong L, Manjappa M, Xu N, Al-Naib I, Zhang W, Singh R (2015) Fano resonances in terahertz metasurfaces: a figure of

- merit optimization. *Adv Opt Mater* 3:1537–1543. <https://doi.org/10.1002/adom.201500207>
9. Singh R, Cao W, Al-Naib I, Cong L, Withayachumnankul W, Zhang W (2014) Ultrasensitive terahertz sensing with high-Q Fano resonances in metasurfaces. *Appl Phys Lett* 105:171101. <https://doi.org/10.1063/1.4895595>
  10. Chen L, Wei YM, Zang XF, Zhu YM, Zhuang SL (2016) Excitation of dark multipolar plasmonic resonances at terahertz frequencies. *Sci Rep* 6:22027. <https://doi.org/10.1038/srep27324>
  11. Hao F, Sonnefraud Y, Dorpe PV, Maier SA, Halas NJ, Nordlander P (2008) Symmetry breaking in plasmonic nanocavities: subradiant LSPR sensing and a tunable Fano resonance. *Nano Lett* 8:3983–3988. <https://doi.org/10.1021/nl802509r>
  12. Manjappa M, Srivastava YK, Cong L, Al-Naib I, Singh R (2017) Active photoswitching of sharp Fano resonances in THz metadevices. *Adv Mater* 29:1–6. <https://doi.org/10.1002/adma.201603355>
  13. Lim WX, Manjappa M, Srivastava YK, Cong L, Kumar A, Macdonald KF, Singh R (2018) Ultrafast all-optical switching of germanium-based flexible metaphotonic devices. *Adv Mater* 30:1–7. <https://doi.org/10.1002/adma.201705331>
  14. Srivastava YK, Chaturvedi A, Manjappa M, Kumar A, Dayal G, Kloc C, Singh R (2017) MoS<sub>2</sub> for ultrafast all-optical switching and modulation of THz Fano metaphotonic devices. *Adv Opt Mater* 5:1700762. <https://doi.org/10.1002/adom.201700762>
  15. Manjappa M, Srivastava YK, Solanki A, Kumar A, Sum TC, Singh R (2017) Hybrid lead halide perovskites for ultrasensitive photoactive switching in terahertz metamaterial devices. *Adv Mater* 29:1–6. <https://doi.org/10.1002/adma.201605881>
  16. Manjappa M, Solanki A, Kumar A, Sum TC, Singh R (2019) Solution-processed lead iodide for ultrafast all-optical switching of terahertz photonic devices. *Adv Mater* 31:1–9. <https://doi.org/10.1002/adma.201901455>
  17. Cong LQ, Srivastava YK, Zhang HF, Zhang X, Han JG, Singh R (2018) All-optical active THz metasurfaces for ultrafast polarization switching and dynamic beam splitting. *Light Sci Appl* 7:28. <https://doi.org/10.1038/s41377-018-0024-y>
  18. Kroner M, Govorov AO, Remi S, Biedermann B, Seidl S, Badolato A, Petroff PM, Zhang W, Barbour R, Gerardot BD, Warburton RJ, Karrai K (2008) The nonlinear Fano effect. *Nature* 451:311–314. <https://doi.org/10.1038/nature06506>
  19. Zheludev NI, Prosvirnin SL, Papasimakis N, Fedotov VA (2008) Lasing spaser. *Nat Photonics* 2: 351–354. <https://doi.org/10.1038/nphoton.2008.82>
  20. He, XY, Lin FT, Liu F, Shi WZ (2016) Terahertz tunable graphene Fano resonance. *Nanotechnology* 27:485202. <https://doi.org/10.1088/0957-4484/27/48/485202>
  21. Amin M, Farhat M, Bagci H (2003) A dynamically reconfigurable Fano metamaterial through graphene tuning for switching and sensing applications. *Sci Rep* 3:2105. <https://doi.org/10.1038/srep02105>
  22. Kotov OV, Lozovik YE (2016) Dielectric response and novel electromagnetic modes in three-dimensional Dirac semimetal films. *Phys Rev B* 93:235417. <https://doi.org/10.1103/physrevb.93.235417>
  23. Borisenko S, Gibson Q, Evtushinsky D, Zabolotny V, Büchner B, Cava, RJ (2014) Experimental realization of a three-dimensional Dirac semimetal. *Phys Rev Lett* 113:027603. <https://doi.org/10.1103/PhysRevLett.113.027603>
  24. Sun Y, Meng Y, Jiang H, Qin S, Yang Y, Xiu F, Shi Y, Zhu S, Wang F (2019) Dirac semimetal saturable absorber with actively tunable modulation depth. *Opt Lett* 44:582–585. <https://doi.org/10.1364/OL.44.000582>
  25. Chen YL, Liu ZK, Zhou B, Zhang Y, Wang ZJ, Weng HM (2014) Discovery of three-dimensional topological Dirac semimetal, Na<sub>3</sub>Bi. *Science* 343:864–867. <https://doi.org/10.1126/science.1245085>
  26. Lu W, Ge S, Liu X, Lu H, Li C, Lai J, Zhao C, Liao Z, Jia S, Sun D (2017) Ultrafast relaxation dynamics of photoexcited Dirac fermions in the three-dimensional Dirac semimetal Cd<sub>3</sub>As<sub>2</sub>. *Phys Rev B* 95:024303. <https://doi.org/10.1103/physrevb.95.024303>
  27. Liu ZK, Jiang J, Zhou B, Wang ZJ, Zhang Y, Weng HM (2014) A stable three-dimensional topological Dirac semimetal Cd<sub>3</sub>As<sub>2</sub>. *Nat Mater* 13:677–681. <https://doi.org/10.1038/nmat3990>
  28. Chen H, Zhang H, Liu M, Zhao Y, Guo X, Zhang YP (2017) Realization of tunable Plasmon-induced transparency by bright-bright mode coupling in Dirac semimetals. *Opt Mater Express* 7:3397–3407. <https://doi.org/10.1364/OME.7.003397>
  29. Chen H, Zhang H, Liu M, Zhao Y, Guo X, Zhang XY (2018) Tunable multiple Plasmon-induced transparency in three-dimensional Dirac semimetal metamaterials. *Opt Commun* 423:57–62. <https://doi.org/10.1016/j.optcom.2018.04.021>
  30. Sun Y, Liao D, Xu J, Wu Y, Chen L (2020) Active switching of toroidal resonances by using a Dirac semimetal for terahertz communication. *Front Phys* 8:602772. <https://doi.org/10.3389/fphy.2020.602772>
  31. Liu Y, Du Y, Liu W, Shen S, Zhang Y (2019) Tunable Plasmon-induced transparency with ultra-broadband in Dirac semimetal metamaterials. *Plasmonics* 16:1717–1723. <https://doi.org/10.1007/s11468-019-00967-0>
  32. Chen H, Zhang H, Zhao Y, Liu S, Cao M, Zhang YP (2018) Broadband tunable terahertz Plasmon-induced transparency in Dirac semimetals. *Opt Laser Technol* 104:210–215. <https://doi.org/10.1016/j.optlastec.2018.02.034>
  33. Zhao T, Hu M, Lian Z, Zhong R, Gong S, Zhang C, Liu SH (2018) Coherent terahertz Smith-Purcell radiation from Dirac semimetals grating with very deep and narrow slits. *Appl Phys Express* 11:082081. <https://doi.org/10.7567/APEX.11.082081>
  34. Su Y, Lin Q, Zhai X, Wang LL (2018) Enhanced confinement of terahertz surface Plasmon polaritons in bulk Dirac semimetal-insulator-metal waveguides. *Nanoscale Res Lett* 13:1. <https://doi.org/10.1186/s11671-018-2686-z>
  35. Liu GD, Zhai X, Meng HY, Lin Q, Huang Y, Zhao CJ, Wang LL (2018) Dirac semimetals based tunable narrowband absorber at terahertz frequencies. *Opt Express* 26:11471–11480. <https://doi.org/10.1364/oe.26.011471>
  36. Sun Y, Meng Y, Jiang H, Qin S, Yang Y, Xiu F, Wang FQ (2019) Dirac semimetal saturable absorber with actively tunable modulation asymmetry. *Opt Lett* 44:582–585. <https://doi.org/10.1364/OL.44.000582>
  37. Wang T, Cao M, Zhang HY, Zhang YP (2018) Tunable terahertz metamaterial absorber based on Dirac semimetal films. *Appl Opt* 57: 9555–9561. <https://doi.org/10.1364/AO.57.009555>
  38. Chen L, Liao D, Guo X, Zhao J, Zhu YM, Zhuang SL (2019) Terahertz time-domain spectroscopy and micro-cavity components for probing samples: a review, *Frontiers of Information. Technol Electron Eng* 20:591–607. <https://doi.org/10.1631/FITEE.1800633>
  39. Timusk T, Carbotte JP, Homes CC, Basov DN, Sharapov SG (2013) Three-dimensional Dirac fermions in quasicrystals as seen via optical conductivity. *Phys Rev B* 87:235121. <https://doi.org/10.1103/PhysRevB.87.235121>
  40. Lim WX, Manjappa M, Pitchappa P, Singh R (2018) Shaping high-Q planar Fano resonant metamaterials toward futuristic technologies. *Adv Opt Mater* 6:1800502. <https://doi.org/10.1002/adom.201800502>
  41. Al-Naib I (2017) Biomedical sensing with conductively coupled terahertz metamaterial resonators, *IEEEJ Sel Top Quantum Electron* 23:4700405. <https://doi.org/10.1109/JSTQE.2016.2629665>